Journal of Magnetism and Magnetic Materials 473 (2019) 484–489

Contents lists available at ScienceDirect

Journal of Magnetism and Magnetic Materials

journal homepage: www.elsevier.com/locate/jmmm

Large-area GMR bio-sensors based on reverse nucleation switching mechanism

Diqing Su[a], Kai Wu[b], Jian-Ping Wang[b,*]

[a] Department of Chemical Engineering and Materials Science, University of Minnesota, Minneapolis, MN 55455, USA
[b] Department of Electrical and Computer Engineering, University of Minnesota, Minneapolis, MN 55455, USA

ARTICLE INFO

Keywords:
Large-area sensor
Spin valve
Reverse nucleation
Magnetoresistance
Biomarker detection

ABSTRACT

In the past 20 years, several studies have been performed on the detection of biomarkers by the stripe-shaped spin valve sensors, whose sensitivity is limited by their small sensing area and large sensor resistance. In this paper, large-area spin valve sensors with lower aspect ratio are introduced. A reverse nucleation mechanism is proposed to demonstrate the different switching processes in large-area sensors. The simulation results further prove the involvement of reverse nucleation sites during the magnetization reversal. Large-area sensors also exhibit a linear response to the concentration of magnetic nanoparticles with a sensor signal more than 20 times larger than the stripe sensors.

1. Introduction

With the ability to monitor the concentration of various biomarkers, biosensors have been widely used in biomedical applications [1–5]. During the detection process, the quantity of target analyte is converted to either optical or electronic signals that will subsequently be picked up by the sensing elements. However, most of the optical techniques such as fluorescence sensors [6,7]and plasmonic sensors [8,9] are not sensitive enough due to the inherent limit of sensitivity such as photobleaching and crosstalk. As a result, additional amplification methods like polymerase chain reaction (PCR) are required to create a sufficient number of analytes, which further complicates the detection process [10,11]. Furthermore, the performance of these biosensors is also easily influenced by the chemical environment of the sample matrix.

In 1998, Baselt et al. built up a new sensing platform called Bead Array Counter (BARC) based on giant magnetoresistance (GMR) sensors, and demonstrated its potential in monitoring the biomolecular recognition process as well as the detection of biomarkers [12]. Compared to other techniques, magnetic sensors exhibit several advantages such as high sensitivity, low background noise and the compatibility with the current Integrated Circuit (IC) technologies [13]. Consequently, the GMR biosensing technology has developed rapidly from the detection of the simplest biotin-streptavidin interaction [14] to the detection of real biomarkers such as viruses [15,16] and pathogens [17,18]. The detectable sample matrix also evolves from buffer solution only [19–21] to more complex substances such as human urine [22] and human sera [23]. Other magnetic biosensing techniques have also been developed. For example, Tian et al. demonstrated virus detection through the combination of AC susceptometry [24] as well as the optomagnetic readout system [25] with the loop-mediated isothermal amplification (LAMP). Nikitin et al. developed a frequency mixing method to detect the response of superparamagnetic nanoparticles (MNPs) [26]. On the contrary, the fundamental sensing mechanism for GMR sensors almost remains the same during the past 20 years. The GMR sensors are patterned into stripes with high aspect ratio to acquire shape anisotropy. (Fig. 1(a)) As the easy axis is defined along the long edge of the stripe, an external field applied along the short edge will result in a linear transfer curve, which is convenient for the quantification of analytes. However, both the sensitivity and the reliability of the stripe sensors are still not good enough due to the limit in the inherent sensing mechanism such as the non-uniformity of signal vs the particle location as well as the reduced sensing area [27]. Signal statistics is another interesting topic [28]. As an alternative approach, GMR biosensors with large areas and low aspect ratios were fabricated and achieved zeptomole sensitivity [29–31]. A one-dimensional reverse nucleation model was proposed previously by our group to explain the sensing mechanism of large-area sensors [31]. Nevertheless, the different switching processes caused by the reverse nucleation site hasn't been fully demonstrated.

In this paper, we first explored the inherent limit of sensitivity in the stripe-shaped sensors by performing the detection of immunoglobulin G (IgG) protein. Object Oriented Micromagnetic Framework (OOMMF)

* Corresponding author.
E-mail address: jpwang@umn.edu (J.-P. Wang).

https://doi.org/10.1016/j.jmmm.2018.10.112
Received 23 June 2018; Received in revised form 23 October 2018; Accepted 23 October 2018
Available online 24 October 2018
0304-8853/

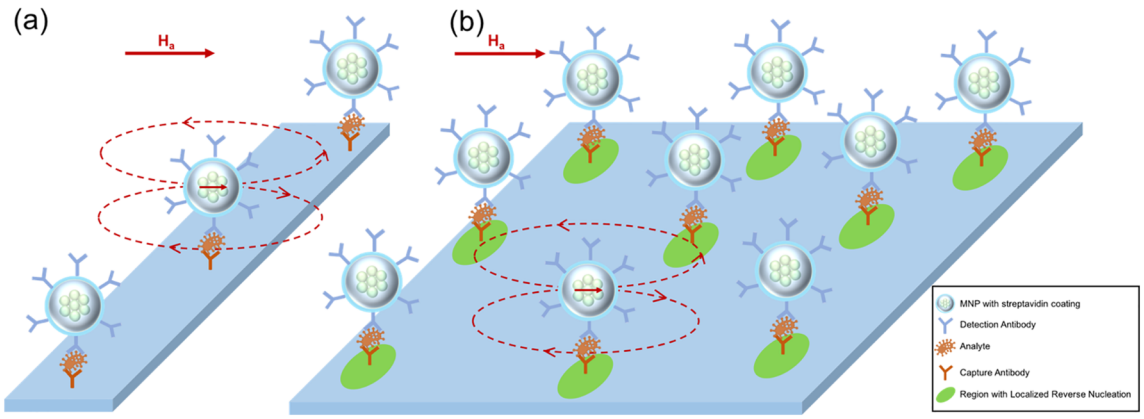

Fig. 1. Schematic illustration of the detection process of (a) Stripe GMR sensors with high aspect ratio; (b) Large-area sensors with localized reverse nucleation sites.

simulations were then carried out to demonstrate the superior sensitivity as well as the role of reverse nucleation sites (Fig. 1(b)) in the magnetization switching process of large-area GMR sensors.

2. Methods

2.1. Fabrication of GMR stripe sensors

GMR stacks with the structure of Ta (5 nm)/NiFe (2 nm)/FeCo (1 nm)/Cu (3 nm)/FeCo (2 nm)/IrMn (8 nm)/Ta (5 nm) were deposited on a Si/SiO_2 wafer by a magnetron sputtering system (Shamrock). The stacks were then patterned into stripe sensors by photolithography and ion milling. Subsequently, 250 nm Au electrodes and 500 nm SiO_2 passivation layer were deposited onto the non-sensing areas on the chip with e-beam evaporation. The rightmost sensor in Fig. 2(b) was also deposited with a SiO_2 passivation layer to serve as the control sensor. The sensing area was covered with an 18 nm Al_2O_3 layer by atomic layer deposition (ALD) and a 15 nm SiO_2 layer by plasma enhanced chemical vapor deposition (PECVD) for protection purpose. The final pattern of the sensors is shown in Fig. 2(b) and (c). Each chip contained 2 sensor arrays. There were 29 sensors in each array. One individual sensor had 24 stripes in it. Each stripe was 150 μm long and 750 nm wide. The chip was annealed under a magnetic field of 398 kA/m along the short edge of the stripe before surface functionalization.

2.2. Detection of IgG protein

After treating with ultraviolet light and ozone (UVO) for 15 min, the chip was immersed in 1% (3-aminopropyl) triethoxysilane (APTES) for one hour. Subsequently, 50 μL 5% glutaraldehyde was dropped on each sensor array. After incubating for 5 h, 1.08 nL 1 mg/mL capture antibody was spotted on each sensor with a liquid dispensing system (sci-FLEXARRAYER S5, Scienion, Germany). The chip was then incubated for 12 h at 4 °C. Two reaction wells with a volume of 50 μL were then assembled onto each sensor array by polydimethylsiloxane (PDMS) (Fig. 2(a)). Subsequently, the sensors were blocked by bovine serum albumin (BSA). 50 μL IgG protein dissolved in phosphate buffer saline (PBS) was then added and incubated for 1 h. After the IgG solution was washed away with PBST (0.05% tween20 in PBS), 50 μL 5 μg/mL biotin-linked detection antibody was added into each well and incubated for 1 h.

During the test, the chip was assembled in a handheld detection system. The baseline was obtained in the first 10 min. Then, MNPs were added to the reaction well and bound to the biotin on the detection antibody. Consequently, the real-time binding curve between the streptavidin on the MNPs and the biotin on the detection antibody was obtained. The sensing scheme is shown in Fig. 1(a). The detailed surface functionalization and detection processes were described in Reference [15].

APTES, BSA, Glutaraldehyde, and IgG were purchased from Sigma-

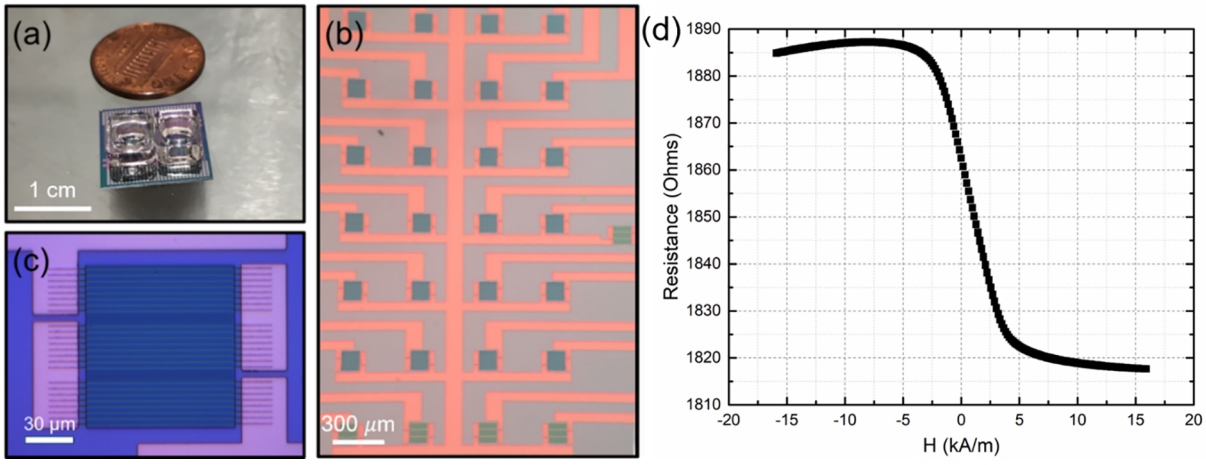

Fig. 2. (a) Image of a GMR chip with two reaction wells. (b) Image of a sensor array in the reaction well. (c) Image of one single sensor. (d) A typical transfer curve of the stripe sensor.

Aldrich, Inc., USA. The anti-mouse IgG functionalized with biotin was purchased from EMD Millipore Corporation, USA and was used as the detection antibody. Streptavidin-coated MNPs (2×10^{12} particles/mL with an average diameter of 50 nm) was purchased from Miltenyi Biotec., Inc., USA, which is referred to as MACS. The MACS consist of multiple 8 nm Fe_2O_3 nanoparticles embedded in a matrix of dextran. The hydrodynamic size of the MACS nanoparticles is 60 nm.

2.3. OOMMF simulation of stripe-shaped and large-area GMR sensors

OOMMF was used to perform micro-magnetic simulation on both stripe-shaped and large-area GMR sensors [32]. The simulation is based on the Landau-Lifshitz-Gilbert equation:

$$\frac{dM}{dt} = -|\gamma|M \times H_{eff} + \frac{\alpha}{M_s}\left(M \times \frac{dM}{dt}\right) \quad (1)$$

where M is the magnetization, α is the Landau and Lifshitz phenomenological damping parameter, H_{eff} is the effective magnetic field, γ is the gyromagnetic ratio, and M_s is the saturation magnetization.

To simulate the detection process, FeCo particles with diameters of 10 nm were put on top of a $4\mu m \times 4\mu m$permalloy thin film or a $20\,nm \times 4\mu m$permalloy stripe with a thickness of 2 nm. FeCo instead of Fe_2O_3 nanoparticles were used here due to their higher M_s, which can reduce the number of MNPs needed on the film surface to generate a readable signal and thus significantly reduce the simulation time. All the MNPs were assumed as single domains. The M-H loops were obtained by applying an external magnetic field between −19.9 kA/m and 19.9 kA/m in 100 steps. The simulation moved on to the next step once the system reached the equilibrium state in the current step. The cell size for the simulation was 5nm × 5nm × 2nm. Other parameters used in the simulation are listed in Table 1.

3. Results and discussion

3.1. Detection of IgG protein with stripe sensors

Stripe-shaped spin valve sensor arrays were used for the detection of IgG protein. The sensor configuration is shown in Fig. 2(a)–(c). Due to the high aspect ratio, the easy axis of the sensor is along the long edge of the stripe, while the applied field is along the short edge of the stripe. A typical transfer curve of the stripes is shown in Fig. 2(d). As the external field is applied perpendicular to the easy axis, a linear relationship between the sensor resistance and applied field is achieved at low fields. Stripe sensor's response to the external field can be characterized by the following equation:

$$R = R_p + \frac{1}{2}MR \bullet R_P(1 - \cos(\theta)) \quad (2)$$

where R is the resistance of the sensor, R_p is the resistance when the magnetizations of the free layer and the fixed layer are in the parallel state, MR is the magnetoresistance of the sensor, and θ is the angle between the magnetization of the free layer and the magnetization of the fixed layer. After the binding of MNPs to the sensor surface, the stray field from the MNPs can be captured by the GMR sensors, which then results in the change of device resistance.

Table 1
Parameters used in OOMMF simulation.

Parameter	Unit (SI)	Value [33,34]	Unit (cgs)	Value
Saturation Magnetization (M_s, *film*, *stripe*)	kA/m	860	emu/cm^3	860
Saturation Magnetization (M_s, *particle*)	kA/m	1900	emu/cm^3	1900
Exchange Constant (A, *particle*, *filmandstripe*)	J/m	1.3×10^{-11}	erg/cm	1.3×10^{-6}
Anisotropy Constant (K, *filmandstripe*)	J/m^3	500	erg/cm^3	5000
Anisotropy Constant (K, *particle*)	J/m^3	10^4	erg/cm^3	10^5
Gilbert Damping Constant (α, *particle*, *filmandstripe*)	1	0.1	1	0.1

The real-time binding signal for different concentrations of IgG protein is shown in Fig. 3. Streptavidin-coated MNPs were added at 12 min. The sensor signal increases as the binding event between the streptavidin on the MNPs and the biotin on the detection antibody occurs and reaches saturation within 10 min. As shown in Fig. 3(a), the sensor signal is represented by the change of magnetoresistance before and after the addition of MNPs, which exhibits a clear trend as the target concentration increases, demonstrating stripe sensors' capability of detecting and quantifying the concentration of biomarkers. When the concentration is below 140 ng/mL (Fig. 3(b)), the sensor signal decreases to less than 800 ppm (1 ppm is equal to a signal change of 10^{-6}), which is comparable to the signal of the control sensor. As a result, the limit of detection for the stripe sensors is restricted in the range of ng/mL, which is consistent with the GMR biosensors reported in other literature values [15,35,36]. It is worth noting that the detection of IgG is performed on a handheld system based on GMR biosensors, which leads to lower sensitivity compared to other benchtop magnetic biosensing mechanisms.

3.2. Intrinsic limit of sensitivity for stripe sensors

The intrinsic limit of sensitivity for stripe sensors mainly originates from three aspects: large noise, small effective sensing area and the sensor signal dependence on the position of the MNPs. At low modulation field frequency, the signal-to-noise ratio (SNR) of the sensor is limited by the flicker noise, which is given by

$$N_f = \frac{\alpha}{Nf}(IR)^2 \quad (3)$$

where N_f is the noise power spectral density, α is the dimensionless Hooge constant, I is the sensing current, f is the field frequency, and N is the total number of conduction electrons in the sensors, which is proportional to the sensing area. From this equation, it can be clearly seen that the flicker noise of the sensor can be reduced by either increasing the sensing area or decreasing the resistance of the sensor. To obtain a higher linearity, the width of the stripe sensors is often scaled down to the sub-micron regime, which not only increases the difficulty of the fabrication process but also reduces the effective sensing area and the number of detectable binding sites. It is also shown that the total sensor signal is not strictly proportional to the number of MNPs bound to the sensor surface. Instead, the MNP stray field experienced by the stripe sensors is highly dependent on the position of the binding sites [27]. More specifically, if the MNPs in the middle of the stripe can generate a positive sensor signal, those on the edge of the stripe will generate a negative signal, resulting in a cancellation of the sensor signal, which further limits the sensitivity of the stripe sensors.

3.3. Sensing mechanism of large-area sensors

One way to overcome the intrinsic limit of sensitivity in stripe sensors is to reduce the aspect ratio, i.e., to increase the sensing area of the spin valve sensors. This not only increases the MNP stray field experienced by the sensor but also reduces the flicker noise. However, the sensing mechanism will also change when large-area spin valve sensors are used. As the aspect ratio decreases, so does shape anisotropy, which makes the local effect in the middle of the film become more important. Here, the OOMMF software is used to simulate the magnetization change under different external fields, where the role of reverse nucleation sites in both large-area sensors and stripe-shaped sensors is discussed.

Different switching behaviors are observed for stripes and large-area films. As shown in Figs. 4(a) and 6(a), (b), domain nucleation and

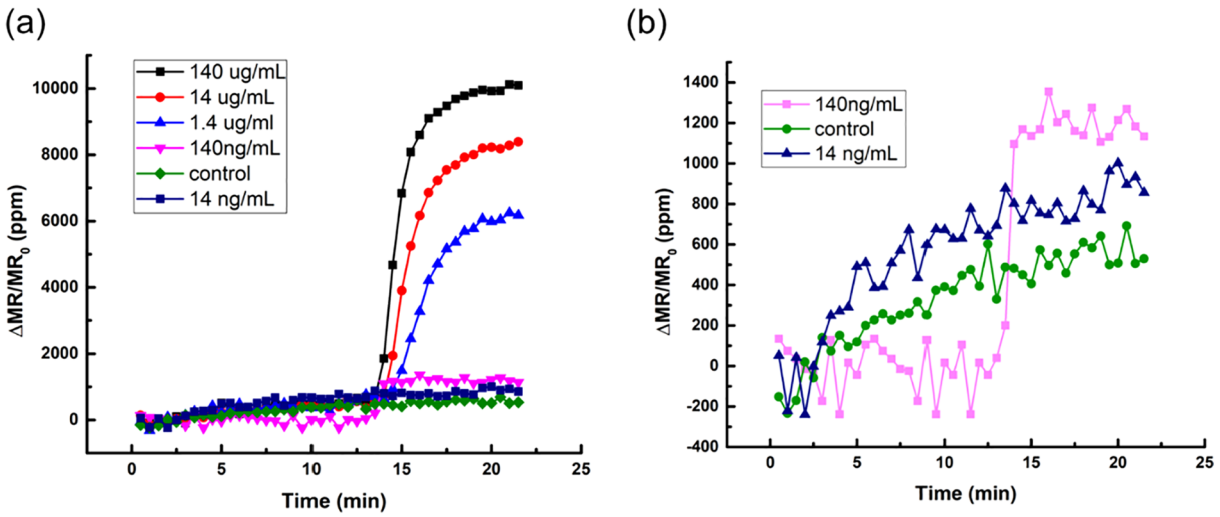

Fig. 3. (a) Real-time binding signal of the sensors for different concentrations of IgG protein. (b) The enlarged real-time binding signal from (a) for concentrations of 140 ng/mL, 14 ng/mL, and the control sensor.

domain wall movement occur in the large-area films either with or without MNPs. For the film with 20 MNPs, when the external field is negative, reverse nucleation sites can be observed under all 20 MNPs. As the stray field from the MNPs is always opposite to the applied field, the rotation of magnetic moments in the reverse nucleation sites will start earlier, resulting in a higher Mx (Figs. 4(b) and 6(b)). The reverse nucleation sites then propagate with the decrease of the negative external field. However, as the external field switches its direction, the reverse nucleation sites become overwhelmed by other domains in the film. In this stage, the domain structure is similar to the film without particles. At higher positive field, the reverse nucleation sites become dominate again, which slows down the saturation of the regions under the MNPs. Compared to large-area films, permalloy stripes exhibit a more coherent switching process when the applied field is perpendicular to the easy axis, which can be attributed to the shape anisotropy (Fig. 5). It is worth noting that the amount and the location of domain walls that form within the stripes are highly dependent on the location of the MNPs, which is the origin of the non-linear relationship between the sensor signal and the MNP concentration shown in Figs. 4(c) and 7(b).

To compare the sensitivity of large-area sensors and stripe sensors, the sensor signal from both configurations is calculated. Here, an external field ranging from −3.18 kA/m to 3.18 kA/m is employed during the detection process, which is comparable to the magnetic field range in the experiments [15]. The sensor signal is defined as $\Delta MR/MR_0$, where MR_0 is the MR of the sensor without the MNPs, and ΔMR is the change of the MR after the addition of MNPs. Based on Eq. (2), the sensor signal can be further rewritten as:

$$\frac{\Delta MR}{MR_0} = \frac{\left(\frac{M_x}{M_{s-40}} - \frac{M_x}{M_{s40}}\right)}{\left(\frac{M_x}{M_{s-40}}' - \frac{M_x}{M_{s40}}'\right)} \cdot \frac{1 + \frac{1}{2}MR\left(1 - \frac{M_x}{M_{s-40}}\right)}{1 + \frac{1}{2}MR\left(1 - \frac{M_x}{M_{s-40}}'\right)} - 1 \quad (4)$$

where $\frac{M_x}{M_{s-40}}$ and $\frac{M_x}{M_{s40}}$ are the averaged magnetizations over the whole sensor at the external field of −3.18 kA/m and 3.18 kA/m before the addition of MNPs, respectively. MR is the magnetoresistance of the sensor at the saturation field. $\frac{M_x}{M_{s40}}'$ and $\frac{M_x}{M_{s-40}}'$ are the magnetizations at 3.18 kA/m and −3.18 kA/m after the addition of the MNPs. The magnetoresistance of the sensor is assumed to be 10%, which is the typical value for the spin valve sensors used in biological detection.

At certain analyte concentration, the number of MNPs bound to the sensor surface per unit sensing area should be constant. Sensor signal vs MNP concentration is plotted in Fig. 7 to illustrate the difference in the sensitivity for large-area sensors and stripe sensors. For large-area sensors, the change in MNP concentration can only influence the number of reverse nucleation sites, while the overall domain structure during the switching process remains the same (Fig. 6(b)), resulting in a linear increase in the sensor signal. In stripe sensors, however, the overall domain structure upon switching is strongly affected by both the concentration and the position of MNPs on the sensor (Fig. 5), which leads to a non-linear increase in the sensor signal. To compare the sensor signal of the sensors at different MNP concentrations, we extrapolate Fig. 7(a) under the assumption that the linearity can be

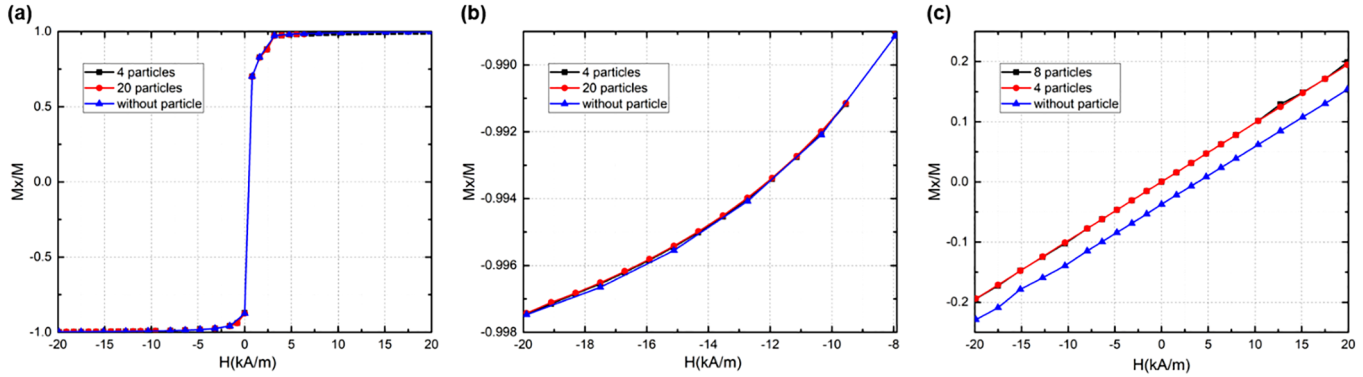

Fig. 4. (a) Simulated MH curves for permalloy thin films with 0, 4 and 20 particles on them. (b) The change of magnetization in a field range of –19.9 kA/m to -8.0 kA/m from (a). (c) Simulated MH loops for permalloy stripes with 0, 4 and 8 particles on them. For all the MH curves, only the ascending branches are shown here.

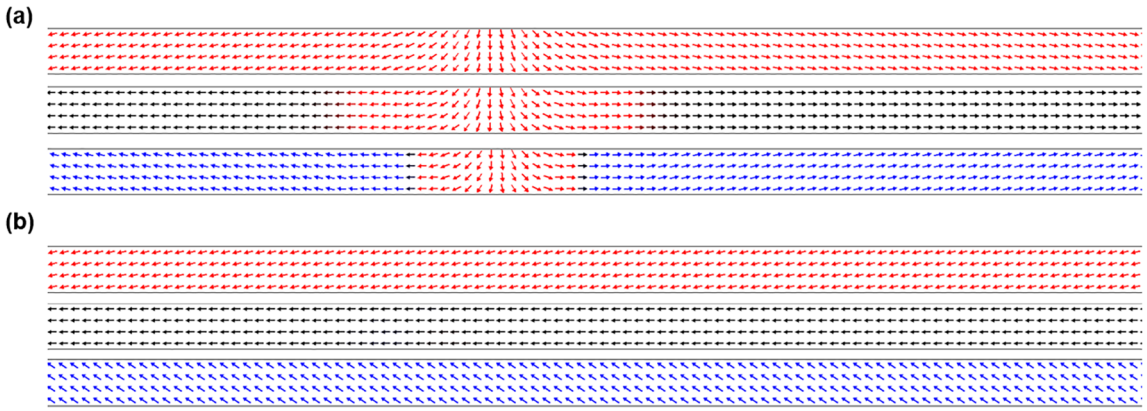

Fig. 5. (a) Magnetization reversal processes in permalloy stripes without MNPs (a) and with 8 MNPs (b). The applied magnetic field is along the y direction, with positive field pointing up (+y direction). The images of magnetizations are taken under external fields of −19.9 kA/m (top), 0 kA/m (middle) and 19.9 kA/m (bottom), respectively. Red arrows indicate the magnetizations with -y components, and blue arrows indicate the magnetizations with +y components. The magnetization distribution of stripe sensors with 4 MNPs are similar to (b), and thus is not shown here. (For interpretation of the references to colour in this figure legend, the reader is referred to the web version of this article.)

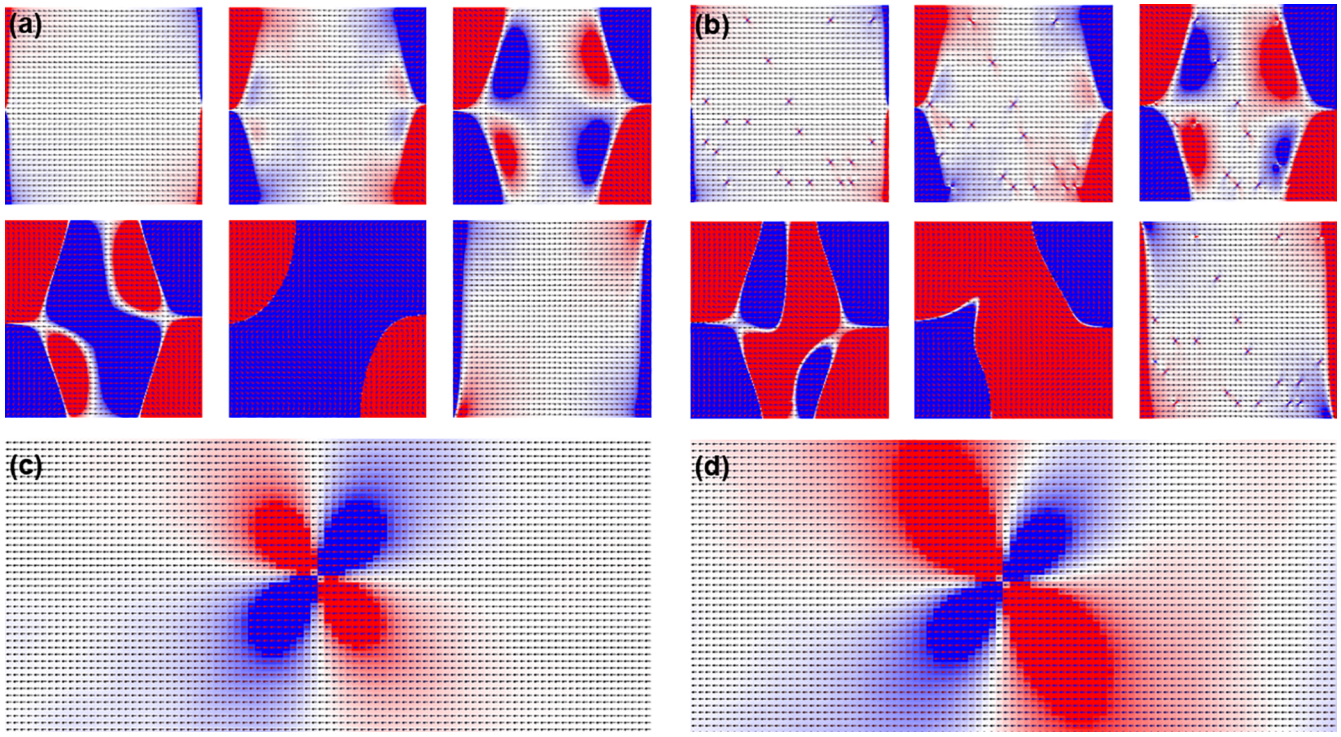

Fig. 6. Magnetization reversal processes in large-area permalloy films without MNPs (a) and with 20 MNPs (b). The large-area film with 4 particles shows similar behavior to (b), and thus is not shown here. In both (a) and (b), the corresponding values of the external field are −15.9 kA/m (upper left), −1.59 kA/m (upper middle), 0 kA/m (upper right), 0.8 kA/m at 3000 iterations (lower left), 0.8 kA/m at 4000 iterations (lower middle) and 7.16 kA/m (lower right). The same reverse nucleation site at −15.9 kA/m (c) and 0 kA/m (d) is also shown. Magnetizations with +y (up) components are marked in red pixels and magnetizations with −y (down) components are marked in blue pixels. Positive external filed is pointing from left to right (+x direction). (For interpretation of the references to colour in this figure legend, the reader is referred to the web version of this article.)

maintained at higher MNP concentrations. The signal from large-area sensors turns out to be 20 times larger than the stripe sensors at the concentration of $50\mu m^{-2}$, and 35 times larger at the concentration of $100\mu m^{-2}$.

4. Conclusions

Although stripe-shaped spin valve sensors have been widely used in biomarker detection, their potential is largely limited by the sensing mechanism. The sensor signal is not only reduced by the small effective sensing area and high noise level, the different sign of the signal from MNPs in the middle and on the edge of the stripes can also cancel with each other, further reducing the SNR. To this end, large-area GMR sensors with low aspect ratios are proposed. The M-H loops for both permalloy stripes and large-area permalloy films with different concentrations of FeCo MNPs are obtained by OOMMF simulation. Reverse nucleation sites can be observed under all the MNPs in large-area sensors before and after the switching process, which leads to a linear increase in sensor signal as MNP concentration increases. The sensor signal of large-area sensors is more than 20 times larger than that of the stripe sensors. Meanwhile, with the smallest feature size increased by hundreds of times, large-area GMR sensors can also simplify the

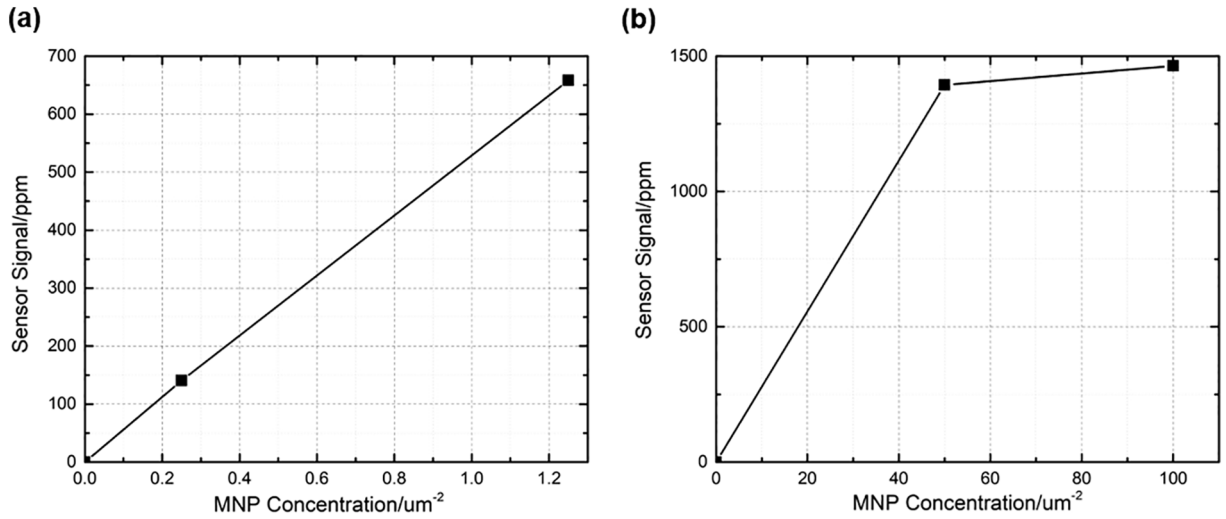

Fig. 7. Sensor signal vs particle concentration for (a) large-area permalloy films and (b) permalloy stripes. The sensor signal is calculated from the MH loops shown in Fig. 4.

fabrication as well as subsequent biological modification processes. Further experiments are needed to justify the simulations and demonstrate the superior performance of the large-area GMR sensors.

Acknowledgements

This work is supported by National Science Foundation MRSEC facility program, Institute of Engineering in Medicine of the University of Minnesota, Centennial Chair Professorship, Robert F Hartmann Endowed Chair, the Distinguished McKnight University Professorship, and UROP program from the University of Minnesota.

Appendix A. Supplementary data

Supplementary data to this article can be found online at https://doi.org/10.1016/j.jmmm.2018.10.112.

References

[1] T. Vo-Dinh, H.N. Wang, J. Scaffidi, J. Biophotonics 3 (2010) 89.
[2] J. Homola, Chem. Rev. 108 (2008) 462.
[3] J.W. Liu, Y. Lu, J. Am. Chem. Soc. 125 (2003) 6642.
[4] B.A. Cornell, V.L.B. BraachMaksvytis, L.G. King, P.D.J. Osman, B. Raguse, L. Wieczorek, R.J. Pace, Nature 387 (1997) 580.
[5] S. Hrapovic, Y.L. Liu, K.B. Male, J.H.T. Luong, Anal. Chem. 76 (2004) 1083.
[6] X.R. Wang, J.M. Hu, G.Y. Zhang, S.Y. Liu, J. Am. Chem. Soc. 136 (2014) 9890.
[7] J.H. Huang, X. Gao, J.J. Jia, J.K. Kim, Z.G. Li, Anal. Chem. 86 (2014) 3209.
[8] D. Rodrigo, O. Limaj, D. Janner, D. Etezadi, F.J.G. de Abajo, V. Pruneri, H. Altug, Science 349 (2015) 165.
[9] X.J. Yang, Y.B. Yu, Z.Q. Gao, ACS Nano 8 (2014) 4902.
[10] N.R. Isola, D.L. Stokes, T. Vo-Dinh, Anal. Chem. 70 (1998) 1352.
[11] J.W.F. Law, N.S. Ab Mutalib, K.G. Chan, L.H. Lee, Front. Microbiol. 5 (2015) 770.
[12] D.R. Baselt, G.U. Lee, M. Natesan, S.W. Metzger, P.E. Sheehan, R.J. Colton, Biosens. Bioelectron. 13 (1998) 731.
[13] J. Schotter, P.B. Kamp, A. Becker, A. Puhler, G. Reiss, H. Bruckl, Biosens. Bioelectron. 19 (2004) 1149.
[14] D.L. Graham, H.A. Ferreira, P.P. Freitas, J.M.S. Cabral, Biosens. Bioelectron. 18 (2003) 483 Pii s0956-5663(02)00205-1.
[15] K. Wu, T. Klein, V.D. Krishna, D.Q. Su, A.M. Perez, J.P. Wang, ACS Sensors 2 (2017) 1594.
[16] V.D. Krishna, K. Wu, A.M. Perez, J.P. Wang, Front. Microbiol. 7 (8) (2016) 400.
[17] X.C. Sun, C. Lei, L. Guo, Y. Zhou, Sensors Actuat. B-Chem. 234 (2016) 485.
[18] P.P. Sharma, et al., Sens. Actuat. B-Chem. 242 (2017) 280.
[19] F.A. Cardoso, J. Germano, R. Ferreira, S. Cardoso, V.C. Martins, P.P. Freitas, M.S. Piedade, L. Sousa, J. Appl. Phys. 103 (2008) 07a310.
[20] D.L. Graham, H. Ferreira, J. Bernardo, P.P. Freitas, J.M.S. Cabral, J. Appl. Phys. 91 (2002) 7786.
[21] S.J. Osterfeld, et al., Proc. Natl. Acad. Sci. U.S.A. 105 (2008) 20637.
[22] B. Srinivasan, Y.P. Li, Y. Jing, C.G. Xing, J. Slaton, J.P. Wang, Anal. Chem. 83 (2011) 2996.
[23] Y.P. Li, B. Srinivasan, Y. Jing, X.F. Yao, M.A. Hugger, J.P. Wang, C.G. Xing, J. Am. Chem. Soc. 132 (2010) 4388.
[24] B. Tian, Z. Qiu, J. Ma, T.Z.G. de la Torre, C. Johansson, P. Svedlindh, M. Stromberg, Biosens. Bioelectron. 86 (2016) 420.
[25] B. Tian, J. Ma, T.Z.G. de la Torre, A. Balint, M. Donolato, M.F. Hansen, P. Svedlindh, M. Stromberg, ACS Sensors 1 (2016) 1228.
[26] P.I. Nikitin, P.M. Vetoshko, T.I. Ksenevich, J. Magn. Magn. Mater. 311 (2007) 445.
[27] T. Klein, Y. Wang, L. Tu, L.N. Yu, Y.L. Feng, W. Wang, J.P. Wang, Sens. Actuat. Phys. 216 (2014) 349.
[28] A.D. Henriksen, M.W.H. Ley, H. Flyvbjerg, M.F. Hansen, PLoS ONE 10 (2015) e0141115.
[29] B. Srinivasan, Y.P. Li, Y. Jing, Y.H. Xu, X.F. Yao, C.G. Xing, J.P. Wang, Angew. Chem. Int. Edn. 48 (2009) 2764.
[30] N. Yang, T. Li, P. Zhang, X. Chen, X. Hu, W. Zhang, J. Nanomed. Nanotechnol. 7 (2015) 1000344.
[31] Y.L. Feng, J.M. Liu, T. Klein, K. Wu, J.P. Wang, J. Appl. Phys. 122 (2017) 123901.
[32] M. Donahue and d. Porter, The Object Oriented MicroMagnetic Framework (Oommf) Project at ITL/NIST. The OOMMF code is Available at http://math.nist.gov/oommf.
[33] Y. Jing, S.H. He, J.P. Wang, IEEE Trans. Magn. 49 (2013) 197.
[34] R.D. Shull, Y.P. Kabanov, V.S. Gornakov, P.J. Chen, V.I. Nikitenko, J. Magn. Magn. Mater. 400 (2016) 191.
[35] S.I. Osterfeld, S.X. Wang, Microarrays: preparation, microfluidics, Detect. Methods Biol. Appl. 299 (2009).
[36] M.Z. Tsai, C.T. Hsiung, Y. Chen, C.S. Huang, H.Y. Hsu, P.Y. Hsieh, Analyst 143 (2018) 503.